On the Origin of the $\sqrt{7} \times \sqrt{7}$ Superstructure and the Anomalous Magnetic and Transport Properties of the Layered Compound $Sr_6V_9S_{22}O_2$

O. Gourdon, M. Evain, S. Jobic,* and R. Brec

Institut des Matériaux Jean Rouxel, Laboratoire de Chimie des Solides, UMR 6502 CNRS−Université de Nantes, 44322 Nantes Cedex 3, France

H.-J. Koo and M.-H. Whangbo*

Department of Chemistry, North Carolina State University, Raleigh, North Carolina 27695-8204

B. Corraze and O. Chauvet*

Institut des Matériaux Jean Rouxel, Laboratoire de Physique Cristalline, UMR 6502 CNRS−Université de Nantes, 44322 Nantes Cedex 3, France

Received December 20, 2000

We examined why the 1T-VS_2 layer of the layered compound $Sr_6V_9S_{22}O_2$ has the $\sqrt{7} \times \sqrt{7}$ superstructure in terms of electronic band structure calculations and metal−metal bonding across the shared edges of adjacent VS_6 octahedra. On the basis of this analysis we explored how the anomalous magnetic and transport properties of $Sr_6V_9S_{22}O_2$ can be explained. Our work shows that the $\sqrt{7} \times \sqrt{7}$ superstructure is not caused by a charge density wave instability associated with Fermi surface nesting but by the metal−metal bonding through the shared edges of adjacent VS_6 octahedra. The weak and strong electron localizations observed for $Sr_6V_9S_{22}O_2$ were discussed in terms of three-center two-electron and two-center two-electron V−V bonds in the 1T-VS_2 layers.

1. Introduction

The 1T-MQ_2 (M = transition metal, Q = O, S, Se, Te) layers made up of edge-sharing MQ_6 octahedra (Figure 1a) exhibit various metal-atom clustering patterns depending on the d-electron count of their transition metal cations.[1,2] For example, the d^0 ions of 1T-TiS_2 exhibit no metal-atom clustering (Figure 1b). The d^2 ions of β-$MoTe_2$, WTe_2, α-ZrI_2, and M′Nb_2Se_4 (M′ = Ti, V, Cr) form zigzag chains (Figure 1c), while those of 1T-MoS_2 and $LiVO_2$ form trimers (Figure 1d). Which clustering pattern a 1T-MQ_2 layer with d^2 metal ions adopts depends on the M−M sigma bonding and the associated lattice strain, both of which are intimately related to the M−Q bond length. In general, the 1T-MQ_2 layers with long M−Q bonds prefer a clustering pattern involving a large metal-atom displacement (i.e., zigzag chains), while those with short M−Q bonds prefers that involving a small metal-atom displacement (i.e., trimers).[2]

The layered compound $Sr_6V_9S_{22}O_2$ reported recently by Litteer et al.[3] possesses interesting structural and physical properties. In this compound two types of layers (i.e., the $Sr_6V_2S_8O_2$ and 1T-VS_2 layers) alternate along the crystallographic c-direction. The $Sr_6V_2S_8O_2$ layer has one $(S_2)^{2-}$ dimer anion, two $(VS_3O)^{3-}$ tetrahedral anions, and six Sr^{2+} cations per unit cell. In the 1T-VS_2 layer the vanadium atoms have a $\sqrt{7} \times \sqrt{7}$ superstructure (Figure 2a) such that a unit cell may be viewed as containing two V_3 "clusters" and one "isolated" V atom. Due to the charge balance for $Sr_6V_9S_{22}O_2$, a unit cell of the 1T-VS_2 layer is represented by $[(VS_2)_7]^{4-}$ and has 11 d-electrons. Consequently, the 1T-VS_2 layer should have at least

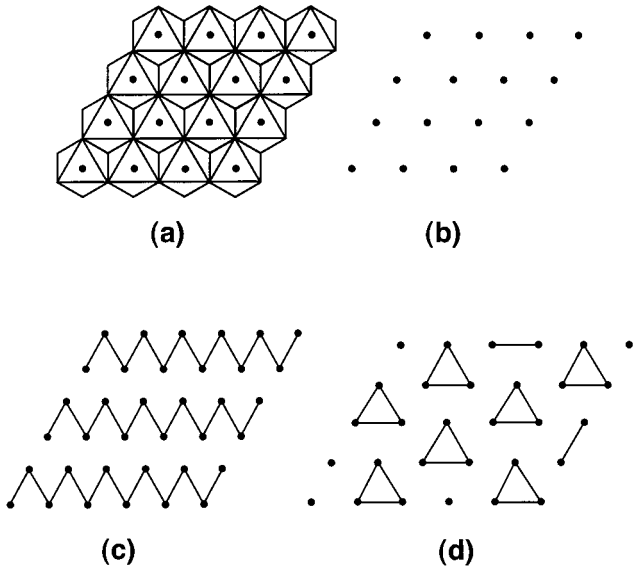

Figure 1. Schematic representations of (a) the 1T-MQ_2 (M = transition metal, Q = O, S, Se, Te) layers made up of edge-sharing MQ_6 octahedra, (b) the hexagonal arrangement of the Ti^{4+} (d^0) ions in 1T-TiS_2, (c) the zigzag chains of the d^2 ions in β-$MoTe_2$, WTe_2, α-ZrI_2 and M′Nb_2Se_4 (M′ = Ti, V, Cr), and (d) the triangular clusters of d^2 ions in 1T-MoS_2 and $LiVO_2$.

(1) Whangbo, M.-H.; Canadell, E. *J. Am. Chem. Soc*. **1992**, *114*, 9587 and references therein.
(2) Rovira, C.; Whangbo, M.-H. *Inorg. Chem*. **1993**, *32*, 4094.
(3) Litteer, J. B.; Chen, B.-H.; Fettinger, J. C.; Eichhorn, B. W.; Lu, H. L.; Green, R. L. *Inorg. Chem*. **2000**, *39*, 458.

10.1021/ic001434y CCC: $20.00
Published on Web 05/10/2001

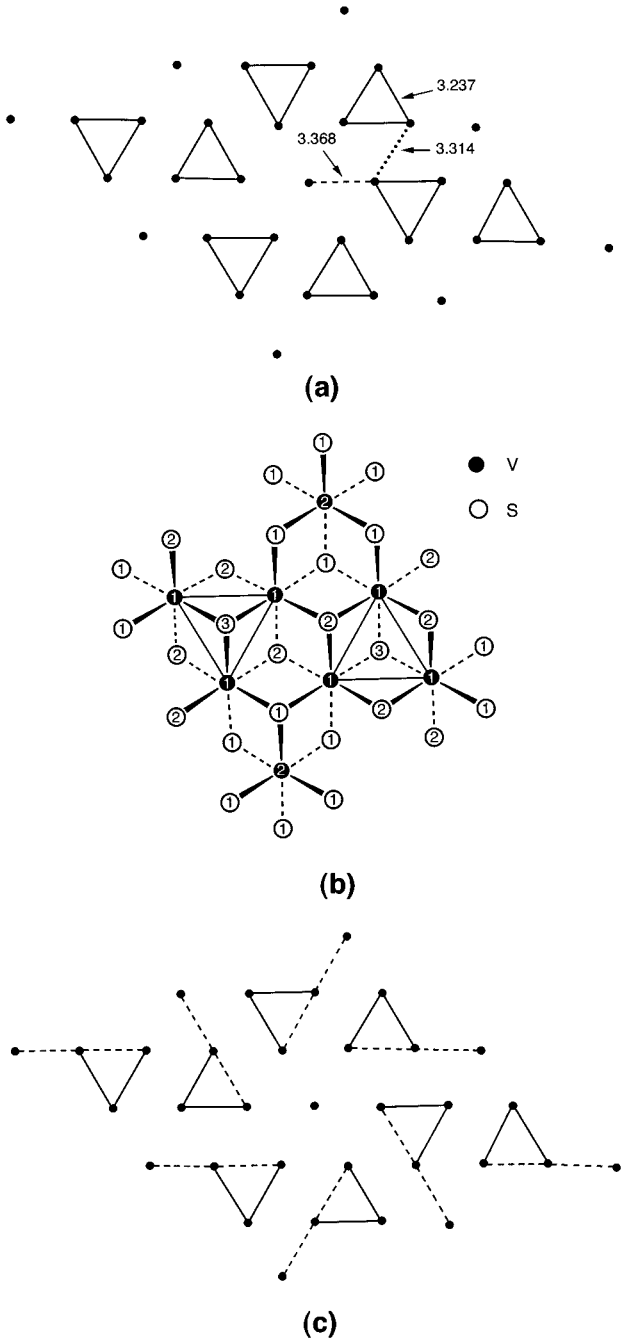

Figure 2. (a) Schematic representation of the $\sqrt{7} \times \sqrt{7}$ superstructure arrangement of the V atoms in the 1T-VS_2 layer, where the isolated dots represent the V(2) atoms, and the dots of the triangles the V(1) atoms. (b) Edge-sharing pattern between adjacent VS_6 octahedra in the 1T-VS_2 layer. (c) Schematic representation of the formation of linear three-center two-electron bond units in the 1T-VS_2 layer, where each solid line between two dots represents a two-center two-electron bond and each dashed line connecting three dots a three-center two-electron bond. The isolated dot in the middle represents an isolated spin site.

one partially filled band so that $Sr_6V_9S_{22}O_2$ is expected to be a metal. This is in apparent disagreement with our measurements of the electrical resistivity of $Sr_6V_9S_{22}O_2$, which is low at room temperature and increases with decreasing temperature (Figure 3a). Nevertheless, from room temperature to ~20 K, the resistivity increases very slowly thereby suggesting that $Sr_6V_9S_{22}O_2$ may be a weakly localized metal in this temperature region. This view is corroborated by the reported magnetic

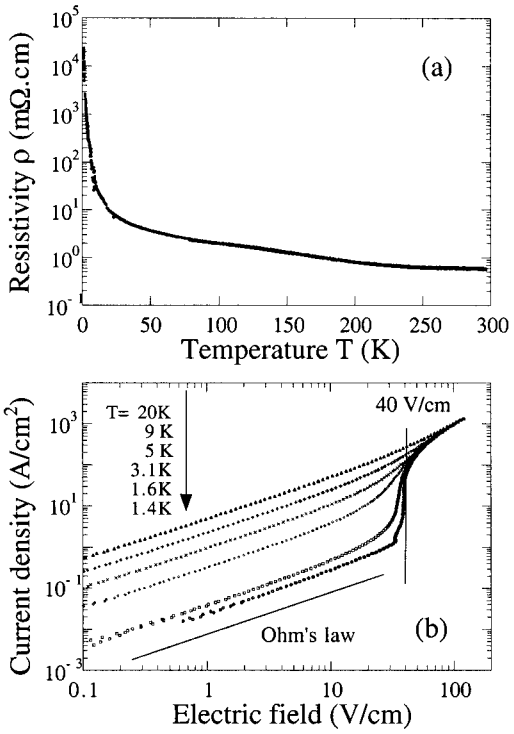

Figure 3. Physical properties of $Sr_6V_9S_{22}O_2$: (a) resistivity vs. temperature and (b) current vs. electrical field strength at low temperatures (from 1.4 to 20 K). The dotted line in (b) indicates the behavior expected from Ohm's law. The threshold field at 20 V/cm is indicated.

susceptibility of $Sr_6V_9S_{22}O_2$,[3] which does not vary significantly in the temperature range between ~30 K and room temperature. As the temperature is lowered below ~20 K, both the resistivity and the magnetic susceptibility increase sharply suggesting the occurrence of a strong electron localization.

In the present work, we examine why the 1T-VS_2 layer of $Sr_6V_9S_{22}O_2$ has the $\sqrt{7} \times \sqrt{7}$ superstructure on the basis of extended Hückel tight binding (EHTB) electronic band structure calculations[4,5] as well as metal−metal sigma bonding across the shared edges of adjacent VS_6 octahedra.[1,2] Then we explore how the anomalous magnetic and transport properties of $Sr_6V_9S_{22}O_2$ can be explained. The atomic orbital parameters employed in the present EHTB calculations are summarized in Table 1.

2. Experimental Section

2.1. Synthesis and Structure Determination. $Sr_6V_9S_{22}O_2$ single crystals were prepared from SrS (Cerac, 99.9%), V_2O_5 (GfE, 99.997%), V (Aldrich, 99.7%), V_2S_3 (Cerac, 99.8%) and S (Fluka, 99.999%) weighted in the 30:2:35:3:71 molar proportions. The reactants were handled in a drybox under nitrogen atmosphere and loaded into a fused silica ampule. The ampule was flame sealed under vacuum and placed in a temperature-controlled tube furnace. The furnace was ramped to 900 °C at 300 °C/h, maintained at this temperature for a week before a cooling back to room temperature in 4 days. The reaction led to the stabilization of platelike crystals with metallic luster. A microprobe analysis by energy-dispersive X-ray spectroscopy gave the chemical composition $Sr_6V_{8.9}S_{22.2}$, and the oxygen content was not quantifiable. The present synthesis procedure is quite similar to that reported by Litteer et al.[3]

(4) Hoffmann, R. *J. Chem. Phys.* **1967**, *39*, 1397.
(5) Our calculations were carried out by employing the *CAESAR* program package (Ren, J.; Liang, W.; Whangbo, M.-H. *Crystal and Electronic Structure Analysis Using CAESAR.*; North Carolina State University: Raleigh, NC, 1998.), http://www. PrimeC.com.

Table 1. Crystallographic Data for $Sr_6V_9S_{22}O_2$

(a) physical, crystallographic, and analytical data	
formula	$Sr_6V_9S_{22}O_2$
crystal color	black
molecular weight (g/mol)	1721.51
crystal system	trigonal
space group (t section)	$R\bar{3}$
temperature (K)	293
cell parameters	
a (Å)	8.7905(5)
c (Å)	34.981(2)
V (Å^3)	2340.9(3)
Z	3
density (calc., g/cm^3)	3.662
crystal description	metallic block
crystal size (mm^3)	$\sim 0.03 \times 0.10 \times 0.20$
(b) data collection	
diffractometer	STOE IPDS
monochromator	oriented graphite (002)
radiation	Mo K$-$L$_{2,3}$ ($\lambda = 0.71073$ Å)
scan mode	ω
no. of measured reflections	10386
hkl range	$-11 < h < 11$ $-11 < k < 11$ $-45 < l < 45$
$\sin(\theta)/\lambda$ range	0$-$0.66
(c) data reduction	
linear absorption coeff. (cm^{-1})	141.6
absorption correction	analytical
T_{min}/T_{max}	0.24/0.65
no. of independent reflections	1241
criterions for observed reflections	$I > 2\sigma(I)$
R_{int} (obs)	0.044
No. of observed reflections	1031
(d) refinement	
refinement	F^2
F(000)	2409
no. of reflections used in the refinement	1031
R/R_w (obs)[a]	2.11/4.75
R/R_w (all)[a]	2.92/4.95
S (obs/all)	1.01/1.07
no. of refined parameters	60
weighting scheme	$w = 1/(\sigma^2\|F_0\| + (0.015)\|F_0\|^2)$
difference Fourier residues	[-0.6, $+1.5$] e$^-$/Å^3

[a] $R = \sum||F_o| - |F_c||/\sum|F_o|$. $R_w = [\sum w(|F_o|-|F_c|)^2/\sum w|F_o|^2]^{1/2}$.

To thoroughly examine the $\sqrt{7} \times \sqrt{7}$ superstructure and in particular the V$-$V distances in the VS_2 layer, a new structure determination was initiated. Data collections were carried out with a single crystal of approximately $0.03 \times 0.10 \times 0.20$ mm^3 in size on a STOE Imaging Plate Diffraction System (IPDS)[6] using graphite-monochromatized Mo K$-$L$_{2,3}$ radiation ($\lambda = 0.71073$ Å). Data intensities were corrected for Lorentz polarization and absorption (Gaussian analytical correction) and subsequently merged according to the $\bar{3}$ point group ($R_{int} = 0.045$ at a 2σ level). With the systematic extinctions suggesting an R centering, the correct space group was confirmed to be $R\bar{3}$ both at the residue factor and at the structure coherence level. The structure was refined (F^2, all reflections included) using the JANA2000 program[7] with the structure of Litteer et al.[3] as the starting point. At the last stage of the refinement, with anisotropic displacement parameters for all atoms, the R factor smoothly converged to $R/R_w = 0.0211/0.0476$ for 1031 reflections with $I/\sigma(I) > 2$ and 59 parameters. This should be compared with $R/R_w = 0.0408/0.1105$ obtained by Litteer et al.[3] under the same conditions. The main crystallographic data, the atomic coordinates, and the anisotropic displacement parameters are listed in Tables 1$-$3. Of the unique atoms listed in Table 2, only the V(1), V(2), S(1), S(2), and S(3) atoms belong to the 1T-VS_2 layer. Table 3 reveals that the vanadium displacement parameters in the 1T-VS_2 layer are significantly larger in the ab-plane than along the c-axis, while the sulfur displacement parameters in the 1T-VS_2 layer are larger along the c-axis than in the ab-plane. The edge-sharing pattern of the 1T-VS_2 layer (Figure 2b) reveals that adjacent V(1)S_6 and V(2)S_6 octahedra share two S(1) atoms, while two adjacent V(1)S_6 octahedra positioned along each V(2)$-$V(1)-V(1) direction share S(2) and S(3) atoms.

Table 2. Fractional Atomic Coordinates and U_{eq} Equivalent Displacement Parameters (Å^2) for $Sr_6V_9S_{22}O_2$

Sr	0.97851(4)	0.38317(4)	0.111464(8)	0.01679(13)
V1	0.85264(7)	0.28757(7)	$-0.000763(14)$	0.0162(2)
V2	1	0	0	0.0187(3)
V3	1	0	0.15280(2)	0.0098(2)
S1	1.04665(9)	0.23796(9)	0.03962(2)	0.0103(2)
S2	0.90278(9)	0.52523(9)	0.040644(19)	0.0098(2)
S3	0.666667	0.333333	$-0.04329(3)$	0.0122(3)
S4	1.01305(10)	0.77460(9)	0.13342(2)	0.0148(3)
S5	1.333333	0.666667	0.13664(5)	0.0273(4)
O	1	0	0.20276(10)	0.0123(9)

2.3. Electrical Resistivity. The electrical resistivity of $Sr_6V_9S_{22}O_2$ was measured on single-crystal samples using the four probe method with silver paste contacts in the temperature range from 1.5 K to room temperature (Figure 3a). Current$-$voltage characteristics are obtained by applying a 100 ms pulse voltage to avoid self-heating (Figure 3b). Two sets of experiments gave essentially the same results. The room-temperature resistivity is of the order of 0.5 mΩ·cm, which is rather low but is not an unexpected value for a metal. From room temperature to $\sim$20 K, the resistivity increases in a logarithmic way. In a two-dimensional (2D) system, this kind of temperature dependence is the signature for a weakly localized metal. This result is corroborated by the magnetic susceptibility measurements of Litteer et al.[3] $Sr_6V_9S_{22}O_2$ exhibits a temperature-independent magnetic susceptibility of 10^{-4} emu/mol, which corresponds to a metallic Pauli paramagnetic susceptibility χ_p of about 1.1×10^{-3} emu/mol when the diamagnetic core contribution is removed (without considering the Van Vleck contribution). This susceptibility suggests that the density of states at the Fermi level, $n(e_f)$, is of the order of 30 states/eV per formula unit according to the relationship $\chi_p = \mu_B^2 n(e_f)$. $Sr_6V_9S_{22}O_2$ has 42 d-electrons states per formula unit $[(VS_2)_7]^{4-}$ in each VS_2 layer. Thus if it is assumed that the t_{2g} bandwidth of each VS_2 layer is about 2 eV, then the $n(e_f)$ value of each VS_2 layer is estimated to be about 21 states/eV per formula unit according to the standard tight binding theory, in approximate agreement with the experimental observation. Thus, in the range between room temperature to $\sim$20 K, $Sr_6V_9S_{22}O_2$ behaves as a weakly localized metal. Below $\sim$20 K, the resistivity increases more steeply upon cooling. The temperature dependence of the electrical resistivity data below 20 K follows a conventional hopping law showing that the system enters a strongly localized regime and does not behave as a metal any more. This temperature regime is associated with a steep increase in the magnetic susceptibility;[3] Litter et al. found a Curie constant of 6.1×10^{-3} emu·K/mol, which amounts to 1.6% spin $^1/_2$ per formula unit. The source of these spins may be paramagnetic impurities in the sample or localized carriers (see below).

3. $\sqrt{7} \times \sqrt{7}$ Superstructure and Metal$-$Metal Sigma Bonding

3.1. Electronic Band Structure. As described in the previous section, $Sr_6V_9S_{22}O_2$ does not behave as a conventional metal. One might speculate if this is due to a charge density wave (CDW) often observed in low-dimensional metals. Let us examine whether the $\sqrt{7} \times \sqrt{7}$ superstructure stems from a CDW instability associated with Fermi surface nesting.[8$-$11] For

(6) *STOE software: Crystal optimization for numerical absorption correction*; Stoe & Cie Gmbh: Darmstadt, Germany, 1996.
(7) Petricek, V.; Dusek, M. *JANA2000: Programs for modulated and composite crystals*; Institute of Physics: Praha, Czech Republic, 1998.
(8) Canadell, E.; Whangbo, M.-H. *Chem. Rev.* **1991**, *91*, 965.
(9) Foury, P.; Pouget, J. P. *Int. J. Mod. Phys. B* **1993**, *7*, 3973.
(10) Dumas, J.; Schlenker, C. *Int. J. Mod. Phys. B* **1993**, *7*, 4045.
(11) Greenblatt, M. *Acc. Chem. Res.* **1996**, *29*, 219.

Table 3. Anisotropic Displacement Parameters U^{ij} (Å^2)[a] for $Sr_6V_9S_{22}O_2$

atom	U^{11}	U^{22}	U^{33}	U^{12}	U^{13}	U^{23}
Sr	0.02231(17)	0.02163(17)	0.01280(13)	0.01542(14)	0.00195(11)	0.00299(11)
V1	0.0203(2)	0.0185(2)	0.0101(2)	0.0097(2)	0.0020(2)	0.0008(2)
V2	0.0242(4)	0.0242(4)	0.0083(5)	0.0121(2)	0	0
V3	0.0107(2)	0.0107(2)	0.0084(3)	0.00533(13)	0	0
S1	0.0090(3)	0.0092(3)	0.0136(3)	0.0050(2)	0.0004(2)	−0.0007(2)
S2	0.0091(3)	0.0091(3)	0.0114(3)	0.0045(2)	−0.0006(2)	0.0006(2)
S3	0.0104(3)	0.0104(3)	0.0163(6)	0.00518(18)	0	0
S4	0.0149(3)	0.0128(3)	0.0170(3)	0.0067(3)	0.0019(2)	−0.0016(2)
S5	0.0222(4)	0.0222(4)	0.0379(8)	0.0111(2)	0	0
O	0.0102(10)	0.0102(10)	0.0171(17)	0.0051(5)	0	0

[a] The anisotropic displacement factor exponent takes the following form:

$$-2\pi^2 \sum_i \sum_j U^{ij} a^i a^j h_i h_j$$

Table 4. Exponents ζ_i and Valence Shell Ionization Potentials H_{ii} of Slater-type Orbitals χ_i Used for Extended Hückel Tight-binding Calculations[a]

atom	χ_i	H_{ii} (eV)	ζ_i	c_1[b]	ζ_i'	c_2[b]
V	4s	−8.81	1.300	1.0		
V	4p	−5.52	1.300	1.0		
V	3d	−11.0	4.750	0.4755	1.700	0.7052
S	2s	−20.0	2.122	1.0		
S	2p	−13.3	1.827	1.0		

[a] The H_{ii}s are the diagonal matrix elements $\langle\chi_i|H^{eff}|\chi_i\rangle$, where H^{eff} is the effective Hamiltonian. In our calculations of the off-diagonal matrix elements $H^{eff} = \langle\chi_i|H^{eff}|\chi_j\rangle$, the weighted formula was used. See: Ammeter, J.; Bürgi, H.-B.; Thibeault, J.; Hoffmann, R. *J. Am. Chem. Soc*. **1978**, *100*, 3686. [b] Contraction coefficients used in the double-ζ Slater-type orbital.

this purpose it is necessary to construct an ideal 1T-VS_2 layer with no superstructure. We define an ideal VS_6 octahedron in terms of the average V−S bond length and ∠S−V−S bond angles obtained from the V(1)S_6 and V(2)S_6 octahedra of the 1T-VS_2 layer with the $\sqrt{7} \times \sqrt{7}$ superstructure. We then construct the ideal 1T-VS_2 layer sharing the edges of such ideal VS_6 octahedra so that the unit cell of the resulting ideal 1T-VS_2 layer is represented by $(VS_2)^{4/7-}$. The dispersion relations and the density of states calculated for the ideal 1T-VS_2 layer using the EHTB method are presented in Figures 4a and 4b, respectively, where only the t_{2g}-block bands are shown for simplicity. With 11/7 electrons to fill the d-block bands, the bottom t_{2g}-block band is partially filled (Figure 4a). Figure 4c shows the Fermi surface associated with this band, which consists of a large triangular hole-pocket centered at K = (2a*/3, 2b*/3) and a small circular hole-pocket centered at Γ = (0, 0). Adjacent triangular pieces of the Fermi surface are partially nested by the vectors $\mathbf{q}_1 \approx \mathbf{a}^*/3 + \mathbf{b}^*/3$, $\mathbf{q}_2 \approx -2\mathbf{a}^*/3 + \mathbf{b}^*/3$, and $\mathbf{q}_3 \approx -\mathbf{a}^*/3 + 2\mathbf{b}^*/3$. A CDW associated with such nesting vectors is expected to triple the unit cell along the a- and b-axes and hence cannot give rise to the $\sqrt{7} \times \sqrt{7}$ superstructure. Consequently, the $\sqrt{7} \times \sqrt{7}$ superstructure cannot be explained in terms of Fermi surface nesting.

The dispersion relations and the density of states calculated for the real 1T-VS_2 layer with the $\sqrt{7} \times \sqrt{7}$ superstructure are presented in Figure 5a and b, respectively, where only the t_{2g}-block bands are presented for simplicity. This distorted layer has partially filled bands so that $Sr_6V_9S_{22}O_2$ is predicted to be a metal. The Fermi surfaces associated with the partially filled bands of Figure 5a are shown in Figure 5c. The Fermi surfaces of the 1T-VS_2 layer with the $\sqrt{7} \times \sqrt{7}$ superstructure are similar to those of the ideal 1T-VS_2 layer in that they exhibit partial nesting between adjacent "triangular" pieces ($\mathbf{q}_1 \approx -\mathbf{a}^*/2 + 2\mathbf{b}^*/3$, $\mathbf{q}_2 \approx -2\mathbf{a}^*/3 + \mathbf{b}^*/9$, and $\mathbf{q}_3 \approx -\mathbf{a}^*/9 + \mathbf{b}^*/2$). The CDW associated with such a partial nesting would lead to a metal-to-metal phase transition,[8−11] but this is not observed experimentally. Consequently, a CDW instability cannot be a cause for the localization found for $Sr_6V_9S_{22}O_2$.

3.2. Two-Center Two-Electron Bonding and Metal−Atom Clustering. We now consider the metal-atom clustering pattern of the $\sqrt{7} \times \sqrt{7}$ superstructure in the 1T-VS_2 layer in terms of metal−metal sigma bonding that occurs through the shared edges neighboring VS_6 octahedra. In general, a MQ_6 octahedron can be viewed in terms of the three basal planes each containing one t_{2g}-orbital (Figure 6a−c). Thus a 1T-MQ_2 layer can be regarded as made up of *trans* edge-sharing MQ_4 chains,[1] as illustrated in Figures 7a−c. The t_{2g}-orbitals contained in the basal plane of each *trans* edge-sharing MQ_4 chain give rise to sigma-type orbital interactions through the shared edges. For example, Figure 8a depicts that the t_{2g}-orbitals of two adjacent metal ions lead to the sigma-bonding and sigma-antibonding levels (σ and σ^*, respectively). Then, a two-center two-electron M−M bond is formed when the σ level is occupied with two electrons. If each metal ion of a 1T-MQ_2 layer has two d-electrons, it can make two such metal−metal bonds with its two adjacent metal ions to form either zigzag chains (Figure 1c) or isolated triangular clusters (Figure 1d).

The 1T-VS_2 layer of $Sr_6V_9S_{22}O_2$ has two types of vanadium atoms, i.e., V(1) and V(2) (Figure 2a); the V(1) atoms form V_3 clusters while the V(2) atoms are isolated. The average V(1)−S bond length of each V(1)S_6 octahedron is slightly shorter than that of each V(2)S_6 octahedron (2.3679 versus 2.3905 Å). According to the gross populations obtained from our electronic band structure calculations, the electron density on the V(2) atom is smaller than that on the V(1) atom (by 0.52 electron). This is consistent with the result of bond valence sum calculations[12] that V(2) has a higher oxidation state than does V(1) (i.e., +3.89 versus +3.66 using the V−S bond valence parameter of 2.208 Å). (Here it is noted that the electron density residing in the V−V metal bonds is neglected in the bond valence sum analysis.) Thus it is reasonable to assign the oxidation state V^{4+} (d^1) for V(2). Then the oxidation state of V(1) becomes $V^{10/3+}$ ($d^{5/3}$), so that each V_3 cluster has five d-electrons. As discussed above, each V−V bond of a V_3 cluster will have σ and σ^* levels. Therefore in each V_3 cluster two σ levels are each doubly filled and the remaining σ level is singly filled. Because the V_3 triangle is equilateral, the three V(1)−V(1) bonds of a V_3 cluster must have an equal probability of having its σ-level singly filled. The latter can be achieved as a consequence of dynamic process

(12) Brown, I. D.; Altermatt, D. *Acta Crystallogr. B* **1985**, *41*, 244.

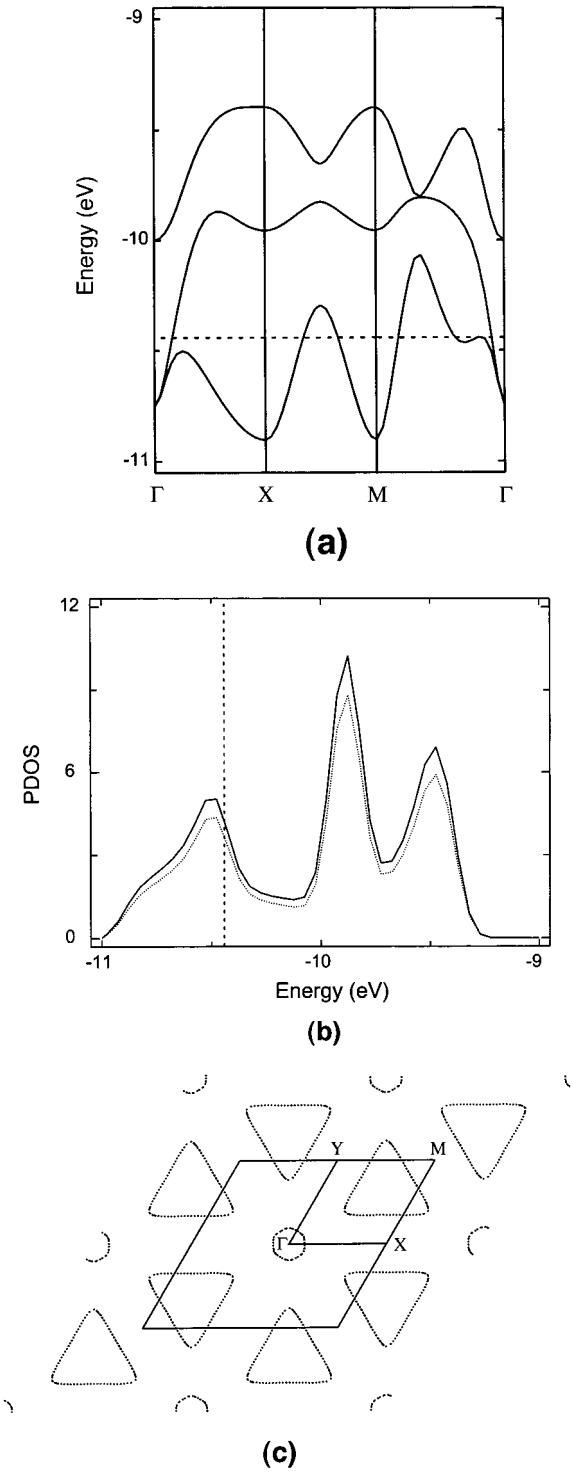

Figure 4. Electronic structure calculated for the ideal 1T-VS_2 layer: (a) the dispersion relations of the t_{2g}-block bands, (b) the density of states of the t_{2g}-block bands, and (c) the Fermi surface. In (b) the solid line refers to the total density of states, and the dotted line the projected density of states for the V 3d orbitals. In (a) and (c), Γ = (0, 0), X = (a*/2, 0), Y = (0, b*/2) and M = (a*/2, b*/2).

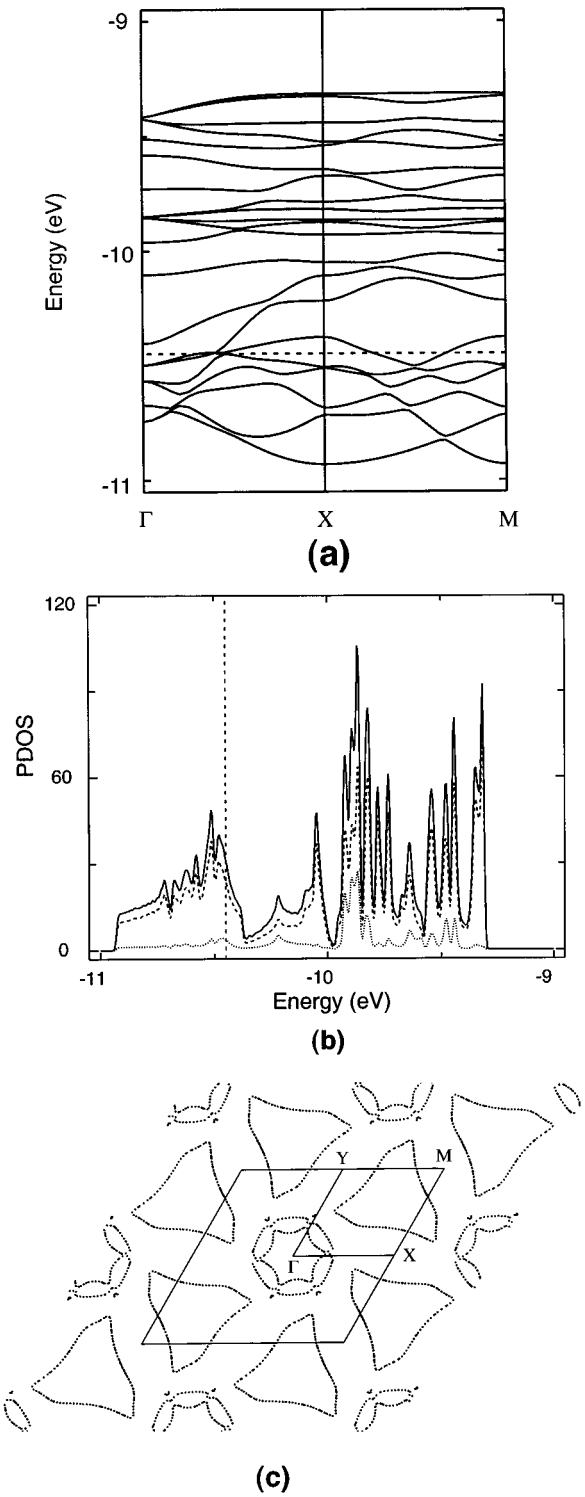

Figure 5. Electronic structure calculated for the real 1T-VS_2 layer with the $\sqrt{7} \times \sqrt{7}$ superstructure: (a) the dispersion relations of the t_{2g}-block bands, (b) the density of states of the t_{2g}-block bands, and (c) the Fermi surface. In (b) the solid line refers to the total density of states, while the dotted and dashed lines represent the projected density of states for the 3d orbitals of the V(2) and V(1) atoms, respectively. In (a) and (c), Γ = (0, 0), X = (a*/2, 0), Y = (0, b*/2), and M = (a*/2, b*/2).

of electron−lattice coupling (Figure 2c), as discussed in the next section.

4. Electron Localization and Three-center Two-electron Bonds

Let us first recall the concepts of weak and strong localizations. In a normal metal, the charge carriers are delocalized and their wave functions extend over the whole crystal from the viewpoint of electronic band structure theory. However, the carriers experience inelastic scattering against phonons, defects, and other electrons, so that the resistivity of a normal metal becomes finite and the average length an electron can travel

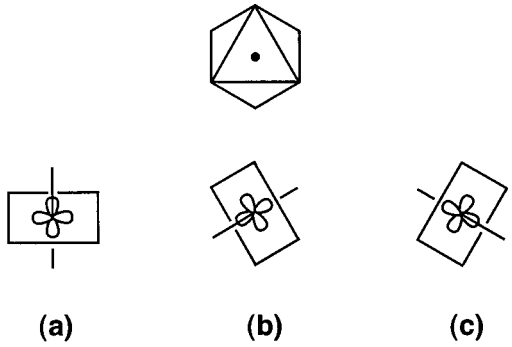

Figure 6. Schematic representations of the three basal planes of a MQ_6 octahedron, where each basal plane contains one t_{2g}-orbital.

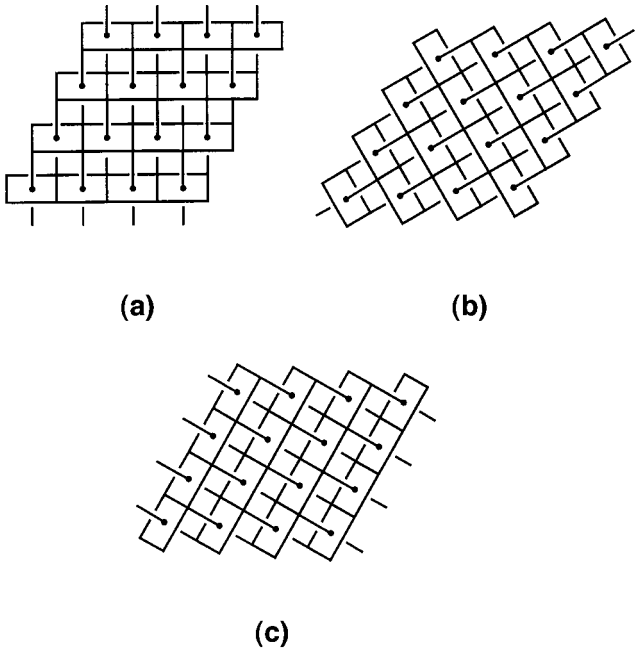

Figure 7. Three views of a 1T-MQ_2 layer in terms of trans edge-sharing MQ_4 chains.

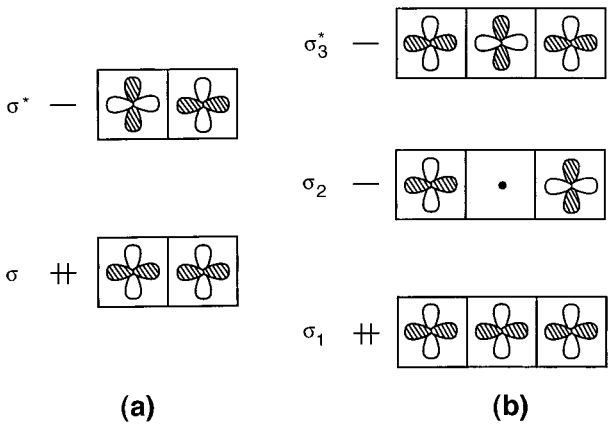

Figure 8. Schematic representations of the sigma-type orbital interactions that occur through the shared edges of the trans edge-sharing MQ_4 chains in the 1T-MQ_2 layer: (a) M_2 dimer and (b) M_3 trimer.

between two inelastic scattering events (i.e., the scattering length l_{in}) becomes finite. A system with partially filled bands can be a metal but is subject to electron localization induced by electron−electron repulsion (Mott−Hubbard localization),[13] by random potential (Anderson localization) associated with lattice defects,[14] or by electron−phonon coupling as found for polaronic states.[15] Electron localization causes the extent of the electron wave function to have a finite length L. If this localization length L is short, the electrons are strongly localized so that the system behaves as an insulator, its charge transport occurs through hopping, and its resistivity increases strongly with decreasing the temperature. In a weakly disordered system, however, the localization length L can be long and even longer than the inelastic scattering length l_{in}. In this case the system acts as a disordered metal so that its resistivity increases slowly with decreasing temperature (in a logarithmic way for a 2D system). The width of the t_{2g}-block bands of the 1T-VS_2 layer is substantial, and the crystal structure refinement for $Sr_6V_9S_{22}O_2$ does not hint any possible random potential. Therefore, both Mott−Hubbard and Anderson localizations are unlikely, and it is of importance to find a probable cause for the weak localization in $Sr_6V_9S_{22}O_2$ between ~20 K and room temperature.

As discussed in the previous section, a unit cell of the 1T-VS_2 layer has one isolated d^1 site (i.e., the V(2) site) and two V_3 clusters each with five d-electrons. Two σ bonding levels of a V_3 cluster are doubly occupied while the remaining σ bonding level is singly occupied. One way of introducing electron localization in the 1T-VS_2 layer is to pair up the electron at each isolated V(2) site with that in the singly filled σ bonding level in one of the neighboring six V(1)−V(1) bonds by forming a linear V(2)−V(1)−V(1) unit (Figure 2c). As depicted in Figure 8b, the orbital interactions associated with such a unit gives rise to three sigma levels, σ_1, σ_2 and σ_3*. With two electrons to fill these levels, the three-center bonding level σ_1 is doubly filled. In this way the d-electrons of the 1T-VS_2 layer can be accommodated into two-center two-electron and linear three-center two-electron bonds. It should be noted that each isolated V(2) atom can make a linear three-center two-electron bond with one of its six nearest-neighbor V(1)−V(1) units.

In the temperature region between ~20 K and room temperature, we envision that the formation and breaking of such three-center two-electron bonds are dynamic without any long-range order. The formation of three-center two-electron bonds would induce lattice distortion, though instantaneous. In such a case these lattice distortions act as inelastic scattering centers for the charge carriers and lead to the localization of the charge carriers. Our transport measurements suggest that the localization length L is longer than the elastic scattering length l_{in}, putting the system in the weakly localized regime. The dynamic process will be frozen if the temperature is lowered such that the minimum energy needed for breaking a three-center two-electron bonding cannot be supplied by the thermal energy. It is likely that the strong localization observed for $Sr_6V_9S_{22}O_2$ below ~20 K reflects such a phenomenon. Once formed below ~20 K, three-center two-electron bonds may be frozen without any long-range order between them. This would lead to "kinks" in the lattice, i.e., spin sites that remain unpaired (e.g., an isolated V(2) site as illustrated in Figure 2c and a V(1)−V(1) bonds with singly filled σ bonding level). Such isolated spin sites would be responsible for the sharp magnetic susceptibility increase of $Sr_6V_9S_{22}O_2$ observed below ~20 K.

All the V−V distances of the 1T-VS_2 layer are longer than 3 Å (Figure 2a) so that the two- and three-center two-electron bonds discussed above should not be taken literally but be

(13) Mott, N. F. *Metal−Insulator Transitions*, 2nd ed.; Taylor & Francis: New York, 1990.
(14) Hayes, W.; Stoneham, A. M. *Defects and Defect Processes in Nonmetallic Solids*; Wiley: New York, 1985.
(15) Schlenker, C.; Marezio, M. *Philos. Mag. B* **1980**, *42*, 453.

regarded as qualitative electron-counting units. Nevertheless, if the dynamic process of electron−lattice coupling presented above (Figure 2c) were to take place, the vanadium atoms of the 1T-VS_2 layer should have significantly greater anisotropic displacement parameters in the ab-plane than along the *c*-axis. Table 3 shows that this is indeed the case. For the V−S bond lengths of the 1T-VS_2 layer to remain the same during the lengthening and shortening of the V(1)−V(1) and V(1)−V(2) distances, the sulfur atoms bridging two adjacent vanadium atoms must undergo a displacement motion mainly along the direction perpendicular to the layer. This explains why the sulfur displacement parameters of the 1T-VS_2 layer are larger along the *c*-axis than in the *ab*-plane (Table 3).

5. Anomalous Temperature Dependence of the Current versus Voltage Plots

As shown in Figure 3b, the current vs. voltage curves determined for $Sr_6V_9S_{22}O_2$ show interesting temperature dependence. Above 25 K the current vs. voltage curves obey Ohm's law, i.e., the current increases linearly with voltage. As the temperature lowered below 20 K, the current vs. voltage curve below the region of 40 V/cm is shifted lower than the curve observed above 20 K indicating that the sample's resistance is increased. Ohm's law is still obeyed as long as the applied voltage is lower than 40 V/cm. As the applied voltage approaches 40 V/cm and increases beyond it, a dramatic deviation from Ohm's law is observed. Furthermore the current vs. voltage curves determined at various temperatures below 20 K exhibit a saturation behavior, i.e., they quickly converge to the curve observed above 20 K. Our measurements show that this saturation phenomenon is reversible as a function of the temperature. At present why the saturation phenomenon occurs below 20 K is not clear. Nevertheless we offer the following tentative explanation. The localized electrons may be viewed as statically pinned in the two- and three-center two-electron bonds discussed above. At low temperature the electron transport occurs via hopping as long as the applied voltage remains below 40 V/cm. A sufficiently high electric field (40 V/cm and above) depins the electrons from the two- and three-center two-electron bonds thereby restoring the weakly localized regime in which the electrical resistivity is essentially independent of temperature. The electrical resistivity vs. temperature and the current vs. electric field data suggest that the transition from the strong to weak electron localization takes place in $Sr_6V_9S_{22}O_2$ at ~20 K and that this transition can be induced either thermally or electrically.

6. Concluding Remarks

Our work shows that the $\sqrt{7} \times \sqrt{7}$ superstructure found for the 1T-VS_2 layer of $Sr_6V_9S_{22}O_2$ is not caused by a CDW instability associated with Fermi surface nesting but by the metal−metal bonding that occurs through the shared edges of adjacent VS_6 octahedra. The weak localization observed for $Sr_6V_9S_{22}O_2$ between ~20 K and room temperature is explained in terms of the dynamic formation and breaking of three-center two-electron and two-center two-electron V−V bonds in the 1T-VS_2 layers, and the strong localization below ~20 K in terms of the freezing of this dynamic process. $Sr_6V_9S_{22}O_2$ exhibits anomalous current vs. voltage curves below 20 K, and this phenomenon is consistent with the transition between strong and weak electron localizations proposed in our work. The sharp susceptibility increase observed below 20 K (i.e., in the strongly localized regime) can be explained in terms of the "kinks" (i.e., isolated spin sites) of the crystal lattice that occur when three-center two-electron bonds are frozen below ~20 K.

Acknowledgment. Work at North Carolina State University was supported by the Office of Basic Energy Sciences, Division of Materials Sciences, U. S. Department of Energy, under Grant DE-FG05-86ER45259.

IC001434Y